

1
2
3 **Statistical Characteristics of Raindrop Size Distributions Observed**
4 **in East China during the Asian Summer Monsoon Season using 2D-**
5 **Video Disdrometer and Micro-rain Radar Data**
6

7
8 Long Wen¹, Kun Zhao¹, Guifu Zhang^{1,2}, Ming Xue^{1,2}, Bowen Zhou¹
9 Su Liu¹, Xingchao Chen¹
10

11
12 ¹Key Laboratory of Mesoscale Severe Weather/MOE and School of Atmospheric
13 Sciences, Nanjing University, 163 Xianlin Road, Nanjing 210023, China
14

15 ²Center for Analysis and Prediction of Storms and School of Meteorology, University
16 of Oklahoma, Norman Oklahoma 73072, USA
17

18
19 Submitted to Journal of Geophysical Research-Atmospheres
20

21 Revised January 2016
22

23 Corresponding author address:
24

25 Dr. Kun Zhao

26 Key Laboratory of Mesoscale Severe Weather/MOE,
27 School of Atmospheric Sciences, Nanjing University,
28 163 Xianlin Road, Nanjing 210023, China

29 Email: zhaokun@nju.edu.cn
30

31 Key points:

32 (1) First report of 2DVD and MRR measurements in East China during summer
33 monsoon season.

34 (2) Structure and DSD of convective, stratiform and shallow precipitation types.

35 (3) Intra-summer variation of DSD and radar rainfall estimation relation.
36

37

Abstract

38 The characteristics of raindrop size distributions (DSDs) and vertical structures of
39 rainfall during the Asian summer monsoon season in East China are studied using
40 measurements from a ground-based two-dimensional video disdrometer (2DVD) and a
41 vertically-pointing micro-rain radar (MRR). Based on rainfall intensity and vertical
42 structure of radar reflectivity, the observed rainfall is classified into convective,
43 stratiform and shallow precipitation types. Among them, shallow precipitation has
44 previously been ignored or treated as outliers due to limitations in traditional surface
45 measurements. Using advanced instruments of 2DVD and MMR, the characteristics of
46 shallow precipitation are quantified. Furthermore, summer rainfall in the study region
47 is found to consist mainly of stratiform rain in terms of frequency of occurrence, but is
48 dominated by convective rain in terms of accumulated rainfall amount. Further
49 separation of the summer season into time periods before, during and after the Meiyu
50 season reveals that intra-summer variation of DSDs is mainly due to changes in
51 percentage occurrence of the three precipitation types, while the characteristics of each
52 type remain largely unchanged throughout the summer. Overall, higher raindrop
53 concentrations and smaller diameters are found compared to monsoon precipitation at
54 other locations in Asia. Higher local aerosol concentration is speculated to be the cause.
55 Finally, rainfall estimation relationships using polarimetric radar measurements are
56 derived and discussed. These new relationships agree well with rain gauge
57 measurements and are more accurate than traditional relations, especially at high and
58 low rain rates.

59

60 **1. Introduction**

61 Raindrop size distribution (DSD) is a fundamental microphysical property of
62 precipitation. Understanding the variability of DSD is important for improving
63 quantitative precipitation estimation (QPE) and microphysics parameterization in
64 numerical weather prediction (NWP) models for accurate quantitative precipitation
65 forecast (QPF) [Milbrandt and Yau, 2005; Sun, 2005; Zhang et al., 2006]. For several
66 decades, rain DSDs have been studied around the world using surface disdrometer
67 measurements and are known to vary both spatially and temporally across different
68 precipitation types, climatic regimes and orography [Ulbrich, 1983; Tokay and Short,
69 1996; Testud et al., 2001; Zhang et al., 2001; Bringi et al., 2003; Rosenfeld and Ulbrich,
70 2003]. Various radar-based QPE algorithms have been developed using these DSD
71 observations. These algorithms include Z - R relations and polarimetric radar algorithms,
72 where Z and R are the radar reflectivity factor and rain rate [e.g., Marshall and Palmer,
73 1948; Rosenfeld et al., 1993; Bringi and Chandrasekar, 2001; Ryzhkov et al., 2005; You
74 et al., 2014].

75 The climate in China is deeply influenced by monsoons. During the Asian summer
76 monsoon season (May-August), southerly winds dominate and warm and moist air is
77 transported from the ocean to the continent of China, increasing convective instability
78 in the region. As a result, heavy precipitation episodes occur frequently in South and
79 East China during the monsoon season. A quasi-stationary subtropical front, called the
80 Meiyu front, is a prominent feature in the region [Tao and Chen, 1987]. The Meiyu
81 front establishes its mean position over South China with the onset of the East Asian
82 summer monsoon in the South China Sea, then moves northward to the Yangtze-Huaihe
83 River Basin to establish the commonly known Meiyu season in the region. The
84 Yangtze-Huaihe River Basin Meiyu season typically lasts from mid-June to mid-July,

85 producing persistent heavy rainfall [*Ding and Chan, 2005; Xu et al., 2009; Yu and Li,*
86 2012].

87 The DSDs in the Meiyu season over China have only received limited
88 investigation. Chen et al. [2013] examined the statistical characteristics of DSDs during
89 the Meiyu season using three-year observations from a one-dimensional (1D) laser-
90 optical OTT Particle Size Velocity (PARSIVEL) disdrometer in Nanjing, China. Their
91 results show that the concentration of raindrops is slightly lower, and the median
92 raindrop diameter is higher than those observed in some other subtropical locations and
93 even during Baiu (Meiyu is named Baiu in Japan) in Japan [*Bringi et al., 2006; Chen*
94 *et al., 2013*]. Tang et al. [2014] further examined DSDs in different climatological
95 regions in China, and found that both North and South China have lower raindrop
96 concentrations than East China during the summer.

97 Results from the cited papers are not conclusive. They are mostly limited to using
98 surface disdrometer observations and they were plenty of measurements uncertainties.
99 For example, the PARSIVEL disdrometer used generally underestimates small
100 raindrops and overestimates large drops [*Tokay et al., 2013*]. As such, it can artificially
101 increase the measured median diameter of raindrops. With only surface-based
102 measurements, it is also difficult to investigate the relationship between DSDs and the
103 corresponding vertical structures of precipitation, which is important for DSD
104 characterization. Finally, those studies focus mainly on precipitation during the Meiyu
105 season; whether DSD varies significantly across the pre-Meiyu, Meiyu and post-Meiyu
106 periods remains unknown [*Xu et al., 2009*].

107 To improve the understanding of the dynamics and microphysics of severe
108 convective systems, field campaigns of the OPACC (Observation, Prediction and
109 Analysis of Severe Convection of China) project were conducted in the Yangtze-Huaihe

110 River Basin in East China in the summers of 2014 and 2015. For the first time, a two-
111 dimensional video disdrometer (2DVD) [Schönhuber et al., 2007], a vertically pointing
112 micro rain radar (MRR), and a wind profiler radar (WPR) were collocated to observe
113 the precipitation microphysics in the east China region (Fig. 1). A one-dimensional
114 PARSIVEL disdrometer was also collocated for comparison purpose. The purpose of
115 this study is to examine the precipitation characteristics during the summer monsoon
116 season in East China using this unique dataset. Unlike previous studies that usually
117 separated precipitation into the convective and stratiform types, three types of
118 precipitation (convective, stratiform and shallow) are identified in this study, and their
119 DSDs and vertical structures are quantitatively compared among the pre-Meiyu, Meiyu
120 and post-Meiyu periods. Furthermore, polarimetric rainfall estimators are derived from
121 DSD observations and discussed as well.

122 **2. Data and methods**

123 **2.1 Instruments and dataset**

124 The datasets used in this study were collected at a national weather station in
125 Jiangning, Nanjing from June to August during the 2014 and 2015 OPACC summer
126 field campaigns. Nanjing is located in the Yangtze-Huaihe River Basin of East China,
127 a region strongly influenced by the East Asia Summer Monsoon in the summer. A
128 picture of the field site (31.93°N, 118.90°E) is shown in Fig.1. The MRR and WPR
129 were located nearby on the roof of a building, about 7 m above the ground and 20 m
130 away from the 2DVD. The rain gauge (RG), OTT PARSIVEL and 2DVD were
131 positioned no more than 3 m apart. The 2DVD used was the current third generation
132 version manufactured by Joanneum Research in Graz, Austria (details can be found at
133 www.distrometer.at). It accounts for the drops in the inner part of the measurement inlet
134 only to reduce splash effects. The horizontal imaging resolution of the unit used in this

135 study is approximately 0.2 mm while the vertical resolution is 0.1 – 0.2 mm for
136 raindrops depending on particle terminal velocity [*Schönhuber et al.*, 2007]. The
137 PARSIVEL disdrometer measures 32 bins of diameter from 0 to 25 mm and 32 bins of
138 fall speeds from 0 to 22.4 m s⁻¹ [*Löffler-Mang and Joss*, 2000]. The vertically pointing
139 MRR is a compact 24 GHz K-band frequency-modulated, continuous-wave (FM-CW)
140 Doppler radar [*Peters et al.*, 2002]. It observes 30 vertical levels in the atmosphere with
141 range-gate resolution set to 200 m. It is also capable of determining DSDs from the
142 Doppler spectra utilizing the relation between drop size and terminal fall velocity
143 according to Atlas et al. [1973]. The main limitation of MRR of such retrieval is that it
144 does not account for wind (horizontal or vertical) at any scale. The temporal resolution
145 is 1 min for 2DVD, MRR, PARSIVEL and RG, and 6 min for WPR in this study. In-
146 situ sounding data were collected as well.

147 By screening the time series of DSD data, as well as composite radar reflectivity
148 mosaic and rain gauge data from China Meteorological Administration (CMA), 27
149 precipitation episodes were identified (Fig. 2 and Table 1) for the two summer seasons,
150 including four in the pre-Meiyu period, nine in the Meiyu period and fourteen in the
151 post-Meiyu period. Following Carbone et al. [2002], a precipitation episode is defined
152 as clusters of rain systems (mainly in the form of organized convection such as squall
153 lines, mesoscale convective systems and frontal rainband) which exhibit coherent
154 rainfall patterns, characteristic of propagating events, under a broad range of
155 atmospheric conditions. The Meiyu period in the Yangtze-Huaihe River Basin was
156 between 23 June and 19 July in 2014 and between 24 June and 13 July in 2015, as
157 officially determined by CMA. The pre-Meiyu period is from 1 Jun to a day before the
158 onset of the Meiyu period, and the post-Meiyu period is from the end date of the Meiyu
159 period to 31 August of each year. Figure 2 indicates that the 850 hPa winds during the

160 precipitation periods are predominantly (over 90% of the time) southeasterly to
 161 southwesterly, with those during the Meiyu season being mostly southwesterly. A
 162 similar quality control method as used in Tokay et al. [2013] is used to process the
 163 2DVD observations. For each 1-min data from the 2DVD, if the total number of drops
 164 is less than 10 or a disdrometer-derived rain rate is less than 0.1 mm h^{-1} , it is disregarded;
 165 otherwise it is considered to be a rainy minute. For each 1-min data from the MRR, if
 166 the rain rate observed by 2DVD is less than 0.1 mm h^{-1} , it is then discarded as noise
 167 caused by non-precipitation echo.

168 2.2 Raindrop size distribution

169 When the raindrop size distribution is given, the integral rainfall parameters
 170 including the radar reflectivity factor Z ($\text{mm}^6 \text{ mm}^{-3}$), rain rate R (mm h^{-1}), liquid water
 171 content LWC (g m^{-3}) and the total concentration of raindrops N_t (m^{-3}) are derived

$$172 \quad Z = \sum_{i=1}^L D_i^6 N(D_i) \Delta D_i, \quad (1)$$

$$173 \quad R = \frac{6\pi}{10^4} \sum_{i=1}^L D_i^3 V_i N(D_i) \Delta D_i, \quad (2)$$

$$174 \quad LWC = \frac{\pi}{6000} \sum_{i=1}^L D_i^3 N(D_i) \Delta D_i, \quad (3)$$

$$175 \quad N_t = \sum_{i=1}^L N(D_i) \Delta D_i, \quad (4)$$

176 where L is the total number of bins, D_i (mm) is the equivalent spherical raindrop
 177 diameter for size-bin i , ΔD_i is the corresponding diameter interval (mm) and
 178 V_i (m s^{-1}) is the fall speed for the velocity-bin i . The equivalent-volume diameters are
 179 sorted into size categories of 0.2 mm. The range in tabulated raindrop diameters is 0.1
 180 – 8.1 mm (41 bins), and the velocity bin is changed to match the size bin. V_i is obtained
 181 by averaging measured particle velocities within that size bin. $N(D_i)$ ($\text{mm}^{-1} \text{ m}^{-3}$)

182 represents the number concentration of drops with diameters in the range from $D_i -$
183 $0.5\Delta D_i$ to $D_i + 0.5\Delta D_i$ (per unit size interval).

184 The widely used three-parameter gamma-model DSD [Ulbrich, 1983] represents
185 the observed raindrop spectra reasonably well [Tokay and Short, 1996]. The gamma
186 size distribution is expressed as

$$187 \quad N(D) = N_0 D^\mu \exp(-\Lambda D), \quad (5)$$

188 where D (mm) is the equivalent diameter and $N(D)$ ($\text{m}^{-3} \text{mm}^{-1}$) is the number
189 concentration of raindrops in a unit volume of air and in the unit size interval.
190 N_0 ($\text{mm}^{-1-\mu} \text{m}^{-3}$), Λ (mm^{-1}) and μ (dimensionless) are the concentration, the
191 slope and the shape parameters, respectively. The n th-order moment of the DSDs is
192 expressed as

$$193 \quad M_n = \int_0^{D_{\max}} D^n N(D) dD. \quad (6)$$

194 The mass-weighted mean diameter D_m (mm) equals the ratio of the 4th to the 3rd
195 moment of the size distribution

$$196 \quad D_m = \frac{M_4}{M_3}, \quad (7)$$

197 and the generalized intercept parameter N_w ($\text{mm}^{-1} \text{m}^{-3}$) was computed as [Brangi et al.,
198 2003]

$$199 \quad N_w = \frac{4^4}{\pi \rho_w} \left(\frac{10^3 W}{D_m^4} \right), \quad (8)$$

200 where ρ_w (assumed to be 1.0 g cm^{-3}) is the density of water.

201 The standard deviation of the mass spectrum (σ_m) with respect to D_m is defined as
202 [Ulbrich, 1983]

$$\sigma_m^2 = \frac{\int_0^{D_{\max}} (D - D_m)^2 D^3 N(D) dD}{\int_0^{D_{\max}} D^3 N(D) dD}. \quad (9)$$

Note that D_m , N_w and σ_m are also calculated directly from measured DSD and not by fitting the measurements to the gamma model.

2.3 Polarimetric radar parameters

Polarimetric radar parameters, such as radar reflectivity in horizontal polarization Z_H ($10\log_{10}(Z_h)$) and differential reflectivity Z_{DR} , provide valuable information that can better characterize DSD variability and estimate precipitation. They are most important for improving the accuracy of rainfall estimation. These variables depend on the DSD and the drop scattering amplitudes as follows:

$$Z_{h,v} = \frac{4\lambda^4}{\pi^4 |K_w|^2} \int_{D_{\min}}^{D_{\max}} |f_{hh,vv}(D)|^2 N(D) dD, \quad (10)$$

$$Z_{DR} = 10\log_{10}\left(\frac{Z_h}{Z_v}\right), \quad (11)$$

where λ is the radar wavelength, K_w is the dielectric factor of water and $f_{hh,vv}(D)$ are the backscattering amplitudes of a drop at horizontal or vertical polarization.

The polarimetric radar parameters in Eq. 10-11 were calculated from the observed DSDs by 2DVD using the T-matrix [Ishimaru, 1991] scattering techniques described by Zhang et al. [2001]. Since the effects of temperature on radar observables at S-band are negligibly small [Aydin and Giridhar, 1992], the raindrop temperature was assumed to be 10 °C in this study. The raindrops were also assumed to follow the Brandes axis ratio relation [Brandes et al., 2002].

2.4 Classification of rain types

Previous studies have usually categorized precipitation into stratiform and convective types based on the rainfall intensity and variation measured by surface

225 disdrometers [Tokay and Short, 1996; Testud et al., 2001; Bringi et al., 2003; Chen et
226 al., 2013]. A few researchers suggested a third type of precipitation (named shallow
227 precipitation) based on data from the vertically-pointing radar observations, which are
228 characterized by low cloud top (below 0 °C isotherm) and weak rainfall rate [Fabry and
229 Zawadzki, 1995; Cha et al., 2009]. However, shallow rainfall has generally been
230 ignored or recognized as stratiform rain by surface disdrometer-based classification
231 schemes.

232 In this study, three types of precipitation, including stratiform, convective and
233 shallow, are defined by combining the rainfall intensity and the vertical structure of
234 radar reflectivity measured by the 2DVD and the MRR. Figure 3 presents an example
235 of the measured vertical profile of reflectivity and the time series of the DSDs using the
236 MRR and the 2DVD from 0000 to 2400 UTC 12 July 2014. The convective, stratiform
237 and shallow categories are indicated by red, black and purple bars, respectively, on the
238 top of Fig. 3a. The feature of the shallow rain, as shown in Fig. 3, has a notable
239 difference compared to the convective and stratiform rain. While the bright band is a
240 marked feature of stratiform precipitation, the top of radar echo of shallow rain is too
241 low to reach the melting layer, which means that the precipitation forms directly in
242 liquid form and no melting is present [Fabry and Zawadzki, 1995; Cha et al., 2009].
243 The corresponding DSDs of this shallow rain have a relatively small maximum
244 diameter and high concentration of raindrops with small diameters, indicating
245 distinctions among the microphysical processes of the three precipitation types.

246 The rain type classification scheme is a two-step procedure. First, a method similar
247 to that used in Bringi et al. [2003] and Chen et al. [2013] is used to classify precipitation
248 into stratiform and convective parts. The time rate change of R and the standard
249 deviation, σ_R , observed by 2DVD is used to separate convective from stratiform rain

250 types. Specifically, over at least 10 consecutive 1-min DSD samples, if the R values are
251 higher than 0.5 mm h^{-1} and the standard deviation σ_R is less than 1.5 mm h^{-1} , then the
252 precipitation is classified as stratiform; otherwise if the R values are higher than 5 mm
253 h^{-1} and the standard deviation σ_R is more than 1.5 mm h^{-1} , then it is classified as
254 convective rain. Samples that belong neither to the stratiform nor convective type are
255 excluded from the investigation. Next, similar to Cha et al. [2009] and Fabry and
256 Zawadzki [1995], the time series of vertical reflectivity measured by MRR is used to
257 separate shallow rain from within the stratiform type identified in step 1. Specifically,
258 for the time series of vertical profiles of reflectivity measured by the MRR during the
259 stratiform processes, if the echo top of radar reflectivity is 1 km lower than the level of
260 the 0°C isotherm, then it is recognized as shallow rain. The rest of the precipitation are
261 recognized as stratiform rain.

262 The classification scheme produces 2,701 convective samples, 6,882 stratiform
263 samples and 1,530 shallow samples, as presented in Table 2. The fraction of
264 uncategorized rainfall is about 11.3% in terms of total rainfall contribution and 21.1%
265 in terms of occurrence frequency. The mean rain rates for convective, stratiform and
266 shallow rains are approximately 24.44 , 2.35 and 1.95 mm h^{-1} . The frequency of
267 occurrence and the corresponding contribution to the total categorized rainfall are,
268 respectively, 24.3 % and 77.5 % for convective rain, 61.9 % and 19.0 % for stratiform
269 rain, and 13.8 % and 3.5 % for shallow rain. Note that, although the percentage of
270 shallow rain rainfall is small, shallow convective precipitation plays an important role
271 in the atmospheric circulation and maritime precipitation as revealed by several recent
272 studies [i.e. *Lowenstein et al.*, 2007; *Blyth et al.*, 2013; *Hamada et al.*, 2015; *Thompson*
273 *et al.*, 2015]. Therefore, understanding the microphysics of shallow rain is also
274 important. Over the continent, shallow rainfall has been little studied, and it may have

275 important roles in, e.g., atmospheric energy balance (for example, affecting the vertical
276 distribution of latent heating [Johnson *et al.*, 1999] by moistening the lower troposphere
277 [Masunaga and Kummerow, 2006]), even though its precipitation amount is relatively
278 small.

279 **3. Results and discussion**

280 **3.1 Vertical structure of precipitation**

281 For different types of rain, the microphysical processes during the formation and
282 landing of raindrops are typically different. Therefore, investigating the vertical profiles
283 of radar reflectivity (VPR, reflectivity greater than 15 dBZ) helps to improve the
284 understanding of the microphysical processes of precipitation. Figure 4 presents the
285 VPR in terms of contoured frequency-by-altitude diagrams [CFAD, Yuter and Houze
286 *Jr.*, 1995] for the three different rain types measured by MRR. The level of the 0 °C
287 isotherm (gray line; about 5,226 m from the ground level) is averaged by all the in-situ
288 sounding data, which are three times a day during the precipitation episodes.

289 The convective CFAD in Fig. 4a has a near absence of low reflectivity (<25 dBZ)
290 near the ground. The reflectivity ranges from 25 dBZ to 53 dBZ with an average value
291 of 38 dBZ. The reflectivity decreases dramatically with height, which can be attributed
292 to the strong reflectivity-attenuation in heavy rainfall, as mentioned by Tsai and Yu
293 [2012] and Wen *et al.* [2015]. Therefore, only the data from the lowest heights (~200m)
294 are quantified for convective rain here, in order to avoid the effect of attenuation on the
295 physical explanation of VPR.

296 In contrast to convective rain, the stratiform CFAD in Fig. 4b indicates a frequent
297 occurrence of weak reflectivity below 4.5 km, with a mean value of about 25 dBZ that
298 stays nearly constant with decreasing height, suggesting that the raindrop evaporation
299 and coalescence are in near balance in stratiform rain. The enhanced radar echo area

300 (known as the bright band) has been detected around 4.6 km, which is 0.6 km below
301 the averaged sounding 0 °C isotherm (~ 5,226 m). The top of the bright band can be
302 considered the melting level and the altitude of the 0 °C isotherm [*Glickman, 2000*],
303 which means that the position of 0 °C isotherm indicated by the MRR and sounding
304 agree well with each other. Above that level, the stratiform reflectivity decreases
305 sharply with height to a minimum centered at about 16 dBZ, and an extremely tight
306 frequency distribution within ± 5 dBZ, representing a nearly homogenous field of
307 reflectivity at each level.

308 Compared to the convective and stratiform rain, the reflectivity of shallow rain is
309 the weakest. The shallow CFAD in Fig. 4c implies a distinctive, narrower frequency
310 distribution. The “modal distribution” (> 50% of the maximum frequency in the
311 distribution, see Hence and Houze [2011]) falls in the range of 15 to approximately 22
312 dBZ, with an average value centered at about 18 dBZ. The modal distribution of
313 shallow rain reaches 1.5 km, while the “outlier distribution” (< 50% of the maximum
314 frequency) reaches approximately 3.5 km and extends to about 28 dBZ. The VPR stays
315 nearly constant with height but far below the melting layer, which means that the
316 precipitation forms directly in liquid form and no ice phase is present. In other words,
317 the warm precipitation process is dominant in shallow rain. The corresponding DSDs
318 of this shallow rain have a relatively small maximum diameter and high concentration
319 of raindrops with small diameters near the ground (as will be shown in Fig. 5d).

320 **3.2 Distributions of D_m and N_w**

321 Figure 5 shows the relative frequency histograms of D_m and $\log_{10} N_w$ for the total
322 categorized dataset and for the convective, stratiform and shallow subsets calculated
323 from the 2DVD, as well as three key parameters: mean, standard deviation and
324 skewness. For the total categorized dataset (Fig. 5a), D_m and $\log_{10} N_w$ histograms are

325 both positively skewed. The standard deviations of the histograms are large (0.34 mm
326 for D_m and 0.61 for $\log_{10} N_w$), which suggest a high variability in D_m and N_w . Note that
327 the units of N_w are in $m^{-3} mm^{-1}$ and the Marshall-Palmer value of $\log_{10} N_w$ for
328 exponential shape is 3.9 ($\log_{10} (mm^{-1} m^{-3})$, omitted hereafter). When considering
329 different rain types, it is found that the D_m histograms are all positively skewed, whereas
330 the $\log_{10} N_w$ histograms exhibit negative skewness for shallow rain (see Figs. 5b-d).
331 Shallow rain histograms show higher skewness for both D_m and $\log_{10} N_w$ when
332 compared with convective and stratiform rain. The convective rain histograms of D_m
333 and $\log_{10} N_w$ tend to shift toward the large values relative to stratiform rain histogram,
334 indicating that convective rain has higher D_m and N_w values. Shallow rain has the
335 smallest D_m (highest $\log_{10} N_w$), the mean value of which is about 0.64 mm (4.97),
336 compared with 1.41 mm (4.37) and 1.16 mm (3.78) for convective and stratiform rain,
337 respectively.

338 Figure 6 shows the scatter plot of $\log_{10} N_w$ versus D_m for the three rain types, as
339 well as statistical results from similar climatic regimes (i.e. East China, Japan and
340 Taiwan, where the climates are deeply influenced by EASM) reported by Bringi et al.
341 [2006], Chen and Lin [2009] and Chen et al. [2013]. The two gray rectangles
342 correspond to the maritime and continental convective clusters reported by Bringi et al.
343 [2003]. The convective rain of our study is mostly plotted over the “maritime-cluster,”
344 and only a few points appear in the “continental-cluster” even though Nanjing is located
345 in the inland area. This result indicates that the summer convective rain in East China
346 is more of a maritime nature. The stratiform rain is plotted over a wide range, from 0.5
347 to 3.0 mm for D_m and 2.0 to 5.7 for $\log_{10} N_w$, respectively. Nearly 72% of the stratiform
348 rain appear on the left side of the “stratiform line” (magenta dashed line in Fig. 6) given
349 by Bringi et al. [2003]. The N_w - D_m pair for the total categorized dataset (red cross) is

350 very close to the stratiform line reported by Bringi et al. ([2003]; magenta dashed line),
351 due to the highest population of stratiform in the summer monsoon season (as shown
352 in Table 2). Note that the unusual stratiform points with $D_m \approx 2.0 - 3.0$ mm and \log_{10}
353 $N_w \approx 2.0 - 2.75$ are caused by a squall line, and the understanding of the exact
354 microphysical processes responsible for these points is beyond the scope of this paper.
355 The majority of shallow points is within the area of $D_m \approx 0.5 - 1.0$ mm and $\log_{10} N_w$
356 $\approx 4.0 - 5.8$.

357 The DSDs measured in this study indicate a lower value of D_m and a higher value
358 of $\log_{10} N_w$ (the mean values are 1.15 mm and 4.09) compared with the 2DVD
359 measurements of Baiu (Meiyu in Japan) in Okinawa, Japan ([Bringi et al., 2006]; where
360 the mean values are 1.47 mm and 3.78), and Meiyu in Taiwan during the Southwest
361 Monsoon Experiment (SoWMEX) ([Chen and Lin, 2009]; where the mean values were
362 1.40 mm and 3.55). Given that all three studies use the same type of instrument (i.e.
363 2DVD) to measure the DSDs of precipitation systems within the East Asian Summer
364 Monsoon, assuming minimum inter-annual variations, the differences in the DSD
365 characteristics are likely to be related to the specific geographical locations.

366 One possible reason for such differences could be the aerosol concentration
367 differences across the regions. In East China, especially in the Yangtze River Delta
368 region, the concentration of aerosols is markedly higher [Streets et al., 2008; Liu et al.,
369 2011]. During the Asian summer monsoon season (May-August), abundant moisture is
370 transported from the ocean inland. In the presence of high aerosol concentration
371 therefore plenty of condensation nuclei's, an adequate supply of moisture tends to lead
372 to higher concentrations of smaller raindrops. In contrast, the aerosol concentration is
373 relatively low over the islands of Japan and Taiwan, and fewer but larger raindrops tend
374 to form mainly through collision-coalescence process. It is noted the DSDs from our

375 2DVD measurements are also different from those obtained from the Meiyu season in
376 Nanjing, China using a 1D PARSIVEL disdrometer ([Chen *et al.*, 2013]. The use of
377 different instruments may be the main cause, as will be discussed more later.

378 To investigate the variability of the two parameters with respect to rain types and
379 rain rates, scatter plots of $D_m - R$ and fitted power-law relationships with different rain
380 types are shown in Fig. 7. For both $D_m - R$ and $N_w - R$ (not shown), the exponents in
381 the relationships are positive, suggesting that the D_m and N_w values are enhanced with
382 rain intensity, possibly due to more efficient coalescence and breakup mechanisms
383 [Chen *et al.*, 2013]. It is notable that at high rain rates, the DSDs may reach an
384 equilibrium state where coalescence and breakup of raindrops are in near balance [Hu
385 and Srivastava, 1995]. Under the equilibrium condition, D_m stays at a constant value,
386 and any increase in rain rate is mainly due to an increase in N_w [Bringi and
387 Chandrasekar, 2001]. As can be seen from Fig. 7a, the D_m values approach a stable
388 value around 1.6 – 1.8 mm for $R > 100 \text{ mm h}^{-1}$, indicating that the DSDs may have
389 reached an equilibrium state. The stratiform rain has the largest coefficient and
390 exponent values of $D_m - R$ relation (Fig. 7c) among the three rain types. Hence, for a
391 given rain rate, stratiform rain has the highest D_m values compared with the convective
392 and shallow rain. For example, when R is 20 mm h^{-1} , the D_m values are 1.44 mm, 1.65
393 mm and 0.91 mm for convective, stratiform and shallow rain, respectively. The
394 coefficient and exponent values of the $D_m - R$ relation are slightly lower for the
395 convective rain (Fig. 7b) and the lowest for the shallow rain (Fig. 7d). Moreover, the
396 observed maximum rain rate of shallow rain is only 8.2 mm h^{-1} while the values of D_m
397 are mostly under 1 mm. As a result, the corresponding contribution to the total rainfall
398 (3.5%) is negligible, even though the raindrop concentration of shallow rain is
399 extremely high.

400 3.3 Composite raindrop spectra

401 The characteristics of the DSD shapes of the total categorized dataset and of the
402 three rain types are presented in Fig. 8. The composite drop size spectra are obtained
403 by averaging the instant size spectra for each rain type. The integral rain parameters
404 derived from the composite spectra are listed in Table 3. Note that the maximum
405 possible raindrop diameter is defined as the diameter of the last bin in the composite
406 spectra whose number concentration is greater than $1.0 \times 10^{-3} \text{ m}^{-3} \text{ mm}^{-1}$, as is done
407 in Chen et al. [2013].

408 The composite spectra exhibit similar one-peak distributions in all three rain types
409 (Fig. 8). Nevertheless, there are distinct differences in the DSDs. The maximum
410 raindrop diameter for convective, stratiform and shallow rain is 6.3, 4.5 and 2.9 mm,
411 respectively. When compared to the other two rain types, the convective spectrum has
412 the highest concentrations at all size ranges, resulting in a higher number concentration,
413 a higher rain rate and more rain water content (see Table 3). The peak concentration
414 appears near the low limit of drop size that the disdrometer can measure. The stratiform
415 spectrum is narrower and that of shallow convection is the narrowest. The latter also
416 has much higher concentrations below 1.1 mm, resulting in higher rain water contents
417 (see also Table 3). Due to the unreliability of measurements of small drops under 0.5
418 mm, we will not discuss that part of the spectrum.

419 When compared with the composite raindrop spectrum of Chen et al. [2013], the
420 most obvious difference is that the spectra of our study have higher concentrations of
421 raindrops, especially in small drop size in both stratiform and convective rain type. For
422 reference, the composite spectrum of two years of Meiyu precipitation data obtained
423 from 2DVD and in situ PARSIVEL (the same instrument as that used in Chen et al.
424 [2013]) are also shown at the upper right corner of Fig. 8. As can be seen, the

425 PARSIVEL disdrometer generally underestimates small raindrops and overestimates
426 large drops when compared to that of 2DVD. Tokay et al. [2013] noticed the same in
427 their study. Accordingly, the higher value of $\log_{10} N_w$ and lower value of D_m obtained
428 from 2DVD than those from PARSIVEL mentioned in section 3.2 can at least be partly
429 attributed to the instrument differences.

430 **3.4 Comparison of different periods**

431 To investigate the DSD differences during different precipitation periods, we
432 define the pre-Meiyu, Meiyu and post-Meiyu periods (see Section 2.1). The integral
433 rain parameters of the three periods are derived from the composite spectra and listed
434 in Table 4. Figure 9 shows the percentage occurrence of different rain types during each
435 precipitation period. The occurrence of convective rain stays around 25 – 30 %
436 throughout. Due to the significant increase of shallow rain, the stratiform rain decreases
437 abruptly from nearly 70 % in the pre-Meiyu and Meiyu periods to 55 % in the post-
438 Meiyu period. For the total categorized rainfall (Table 2), the contribution to
439 precipitation amount in the summer monsoon seasons of 2014 and 2015 in the study
440 area is dominated by convective rain (77.5 %) while stratiform rain occurs most
441 frequently (61.9 %). These results are consistent with those of previous studies using
442 three years of ground-based disdrometer data [*Chen et al.*, 2013] or ten years of TRMM
443 PR measurements [*Liu et al.*, 2012].

444 The average values of D_m and $\log_{10} N_w$ for the three rain types during the different
445 precipitation periods are given in Fig. 9 as well. For each rain types, the average D_m
446 and $\log_{10} N_w$ values in pre-Meiyu and Meiyu period show slight difference except that
447 the $\log_{10} N_w$ for shallow rain decrease moderately from 5.14 to 5.00. In post-Meiyu, the
448 average $\log_{10} N_w$ values show moderate increase for convective and stratiform rain and
449 the average D_m values decrease a little for convective rain. Overall, there are no distinct

450 differences in the average D_m and $\log_{10} N_w$ values for each rain type across the different
451 precipitation periods. This suggests that the characteristics of each rain type remain
452 unchanged during the whole monsoon period.

453 The occurrence frequency of various parameters (the mass-weighted diameter D_m ,
454 the generalized intercept parameter N_w , the liquid water content LWC and the standard
455 deviation of the mass spectrum σ_m) are computed to investigate the variability of the
456 four parameters across the pre-Meiyu, Meiyu and post-Meiyu periods. The occurrence
457 frequency is defined as the number of occurrences for a specific value normalized by
458 the total number of samples. As shown in Fig. 10a, D_m decreases from the pre-Meiyu
459 period to the post-Meiyu period. The peak value of the D_m distribution curve appears at
460 1.3 mm for the pre-Meiyu period and at 1.1 mm for the Meiyu period, which is
461 approximately equal to the mean D_m value of the stratiform rain for each period, 1.24
462 mm and 1.18 mm, as given in Fig. 9. Because of the significant increase in shallow rain,
463 double-peak distribution results for the post-Meiyu period, where the values appear at
464 0.7 mm and 1.3 mm. i.e. one peak (1.3 mm) approximately equal to the mean D_m value
465 of the stratiform rain while the other peak (0.7 mm) is attributed to the significant
466 increase in shallow rain during the post-Meiyu period. Similarly, the distribution \log_{10}
467 N_w shows a two-peak pattern for the post-Meiyu period as well, and $\log_{10} N_w$ around
468 the second peak is larger than the other two periods (also see Table 4). However, there
469 are only slight differences in liquid water content (LWC) among the three periods (Fig.
470 10c and Table 4). The Meiyu period shows the lowest LWC values compared to the
471 other periods, as the mean values of LWC are 0.57, 0.44 and 0.50 g m^{-3} for the pre-
472 Meiyu, Meiyu and post-Meiyu periods, respectively. Such variations of LWC can be
473 explained by Eq. (3), where LWC depends on both raindrop diameter ($\sim D^3$) and
474 number concentration $N(D)$. The convective rain has the largest raindrop size, hence

475 the highest LWC among all three types of precipitation. Compared with stratiform rain,
476 shallow rain has a lower D but a higher $N(D)$, so they contain almost the same LWC .
477 As the Meiyu period has the lowest occurrence frequency of convective rain, it
478 therefore has the lowest LWC among three periods. The distribution of σ_m has little
479 difference between the pre-Meiyu and Meiyu periods while the post-Meiyu period
480 shows the narrowest spectrum with the integral distribution becoming narrower and
481 yielding smaller values, due to the abundance of shallow rain.

482 The above analyses indicate that the DSDs of each rain type during the three
483 precipitation periods from summers of 2014 and 2015 differ only slightly. The
484 difference in the occurrence frequency of various DSD parameters for different
485 precipitation periods seems to have been due more to the difference in the dominant
486 precipitation type in each period than to the change in season. Specifically, the pre-
487 Meiyu period contained a higher percentage of convective rain episodes that were
488 associated with well-organized mesoscale convective systems while the Meiyu rainfall
489 had the largest fraction of stratiform rain, and the post-Meiyu period, in contrast, had a
490 significant increase in shallow rain.

491 **3.5 Rainfall estimation relationships**

492 Based on the characteristics of DSDs in the summer monsoon season over East
493 China, radar-based rainfall estimation algorithms are discussed in this section. The most
494 widely used radar QPE algorithm is the Z - R relation. However, the diversity of DSDs
495 due to rain types, geographical locations, climatic regimes, and even the choice of
496 disdrometers, will result in different coefficients in the Z - R relation [*Chandrasekar et*
497 *al.*, 2003; *Rosenfeld and Ulbrich*, 2003; *Tokay et al.*, 2008]. For example, the National
498 Weather Service's (NWS) Weather Surveillance Radar-1988 Doppler precipitation
499 processing subsystem recommends $Z = 250R^{1.2}$ [*Rosenfeld et al.*, 1993] for tropical

500 systems, and Chen et al.[2013] suggests $Z = 368R^{1.21}$ for Meiyu systems. Thus, a better
501 understanding of the characteristics of the DSD in East China during the summer
502 monsoon season is needed to help us improve radar rainfall estimation in this region.

503 Scatter plots between Z and R for the total categorized dataset and for the three
504 rain types are presented in Fig. 11. The coefficient and exponent values of the fitted
505 power-law equations are provided with the corresponding colors. In order to facilitate
506 the comparison of Z - R relation with different rain types, $Z = 368R^{1.21}$ [Chen et al., 2013]
507 for convective rain in Meiyu season and $Z = 200R^{1.6}$ [Marshall and Palmer, 1948] for
508 continental stratiform rain are also provided. The former $Z = 368R^{1.21}$ relationship is
509 slightly to the right of our $Z = 230.85R^{1.34}$ relationship for convective rain at high rain
510 rates. In other words, it gives a higher R value for a given Z , which indicates that $Z =$
511 $368R^{1.21}$ would overestimate rainfall, in particular at high rain rates. For example, when
512 Z is $1.0 \times 10^5 \text{ mm}^6 \text{ m}^{-3}$ (50 dBZ, which happens frequently in summer rainfall), the
513 rain rate is overestimated by about 25% with the former $Z = 368R^{1.21}$ relationship. As
514 shown in Fig. 11, our new $Z = 232.44R^{1.34}$ relationship for the total categorized dataset
515 fits the measured data well, in particular with the new relationship for convective rain,
516 although it underestimates the rainfall at low rain rates. This again suggests that the
517 contribution of precipitation in summer monsoon season is mainly dominated by
518 convective rain.

519 The new relationships for the three rain types are typically different from each
520 other. Although the raindrop concentration is the highest for shallow rain, the new $Z =$
521 $41.68R^{1.68}$ relationship for shallow rain lies to the lower-right of the other two
522 relationships. This is because radar reflectivity is more sensitive to raindrop diameter
523 D than to raindrop concentration $N(D)$, as can be concluded from Eq. (1) or the
524 combination of Figs. 4 and 5. Thus, for a given Z , the shallow Z - R relationship would

525 estimate a higher R value than the stratiform Z - R relationship. The distinct difference
526 between the shallow and stratiform Z - R relationships suggests that there are two
527 different types of precipitation. Furthermore, overestimating rainfall by previous
528 stratiform Z - R relationships might be partly due to the erroneous classification of
529 shallow rain as stratiform rain by surface disdrometer-based schemes.

530 The above analysis, as well as previous studies, suggests that DSD variability is a
531 major source of diversity of Z - R relations. Since the accuracy of remote estimation of
532 rainfall is limited by and progress is impeded by the variety of DSDs and sampling
533 errors, researchers have turned to fixed-form relations of polarimetric measurements
534 which provide additional parameters. Recent studies indicate that rainfall estimates
535 made with the radar reflectivity (Z_H) and differential reflectivity (Z_{DR}) measurement
536 pair are sensitive to size variations. They help to improve rainfall estimates derived only
537 from radar reflectivity [Zhang *et al.*, 2001; Brandes *et al.*, 2002; Ryzhkov *et al.*, 2005;
538 Lee, 2006; Cao *et al.*, 2008; Cao *et al.*, 2010; You *et al.*, 2014]. In this study, S-band
539 polarimetric radar parameters Z_H and Z_{DR} are calculated following Zhang *et al.* [2001]
540 for Brandes drop shape assumption using 2DVD data observed during the summer. A
541 power-law rainfall estimation relationship is then determined by the least squares
542 method and the $R(Z_H, Z_{DR})$ is given by

$$543 \quad R = 1.81 \times 10^{-3} Z_H^{0.968} Z_{DR}^{-0.86}, \quad (12)$$

544 where Z_H ranges from $10^{1.5}$ to $10^{5.6}$ $\text{mm}^6 \text{m}^{-3}$ and Z_{DR} ranges from 0.1 to 3 dB, similar
545 to Aydin and Giridhar [1992].

546 Figure 12 shows the scatter plots of 2DVD observed hourly rainfall against the
547 rainfall from the rainfall estimation relationship $R(Z_H, Z_{DR})$. To ensure a rigorous
548 assessment, no threshold is set for either observed or estimated rainfall. The results of
549 the statistical evaluation are given as well. The correlation coefficient (CC), standard

550 deviation (STD) and root mean square error (RMSE) between $R(Z_H, Z_{DR})$ -estimated and
551 observed rainfall are 0.997, 0.524 and 0.534, respectively. The results suggest that the
552 polarimetric estimates agree well with observations on the whole. These estimates
553 perform well even when low rain rates (where Z_{DR} measurement errors could be
554 important) are included.

555 The disadvantage of the Z - R relation is that it is not unique and depends on DSDs,
556 which vary both spatially and temporally across differing precipitation types, climatic
557 regimes and orography. The $R(Z_H, Z_{DR})$ estimator has the advantage over the single-
558 parameter estimator (Z - R relation) because it partially accounts for changes in median
559 drop size through the Z_{DR} parameter. This capability reduces the impact of DSD
560 variability on the quality of rainfall estimation [Brandes *et al.*, 2002; Ryzhkov *et al.*,
561 2005]. That is to say, without classification of rain types, rainfall estimation is
562 consequently more accurate with additional polarimetric observations.

563 **4. Summary and conclusions**

564 In this paper, the characteristics of the raindrop size distributions (DSDs) and
565 calculated polarimetric radar parameters of precipitation episodes during the Asian
566 summer monsoon season are studied. For the first time, measurements from ground-
567 based 2D video disdrometer and vertically pointing Micro-rain radar are utilized to
568 improve characterization of summer precipitation in East China. A total of 27
569 precipitation episodes and 11,113 1-min DSD spectra are obtained for the summers of
570 2014 and 2015 at a site located in Nanjing in the Yangtze-Huaihe River Basin of East
571 China. Combining the rainfall intensity and the vertical structure of radar reflectivity,
572 convective, stratiform and shallow rain types are identified, and their DSDs and vertical
573 structures are further compared among different precipitation periods (pre-Meiyu,
574 Meiyu and post-Meiyu). Single-polarization and polarimetric rainfall estimators are

575 derived from DSD observations and discussed as well. The main conclusions can be
576 summarized as follows:

577 (1) The use of 2DVD and MRR observations enabled the identification of shallow rain
578 in this study, which had generally been ignored or mistakenly recognized as
579 stratiform rain in previous studies. Compared to the convective and stratiform rain,
580 the reflectivity of shallow rain is the weakest. The vertical profiles of reflectivity
581 shows that the shallow precipitation forms mostly through warm rain processes.
582 The shallow rain DSDs have a relatively small maximum diameter and high
583 concentrations with small diameters near the ground.

584 (2) The rainfall in the two summers studied at the measurement site is found to consist
585 mainly of stratiform rain in terms of frequency of occurrence, but is dominated by
586 convective rain in terms of accumulated rainfall amount. Relatively low values of
587 D_m but high values of N_w are observed for all three rain types when compared with
588 observations from similar climatic regimes (i.e. East China, Japan and Taiwan).
589 This is likely associated with high local atmospheric aerosol and moisture contents.
590 In the presence of high aerosol concentration, adequate supply of moisture leads to
591 a higher raindrop concentration but lower raindrop diameter.

592 (3) The differences of the frequency distributions of various parameters during different
593 precipitation periods appear to be due more to percentage occurrence variations
594 among the three rain types, than to variation within each rain type. In other words,
595 the characteristics of each precipitation type remain largely unchanged during the
596 summer, although they occur at different frequencies before and after Meiyu.

597 (4) Radar-based rainfall estimation algorithms, $R(Z_H)$ and $R(Z_H, Z_{DR})$, are also derived
598 and discussed. The Z - R relationships obtained are $Z = 230.85R^{1.34}$, $Z = 193.73R^{1.54}$,
599 and $Z = 41.68R^{1.68}$ for convective, stratiform and shallow rain, respectively. In

600 comparison, the single polarimetric $R(Z_H, Z_{DR})$ algorithm agrees well with rainfall
601 observations for all rain types. The $R(Z_H, Z_{DR})$ estimator has the advantage over the
602 single-parameter estimator (Z - R relation) because it accounts for DSD differences
603 through the additional Z_{DR} parameter.

604 Although interesting findings were obtained on the DSD characteristics of
605 different types of summer precipitation in East China using two years of data from two
606 types of disdrometer and an MRR, the results are not necessarily conclusive due to the
607 still limited sample size of precipitation events. Long-term observations should be used
608 as more data are collected. The vertical profiles of drop size spectra from MRR can be
609 used to better understand the growth of raindrops in the shallow rain. The aerosol effects
610 on DSDs are not yet well understood [Rosenfeld *et al.*, 2008; May *et al.*, 2011; Tao *et*
611 *al.*, 2012], and aerosol observations are needed to determine the relation between the
612 raindrop size and high-CCN. Moreover, high-resolution simulations with microphysics
613 schemes properly accounting the effects of aerosol will be helpful for understanding
614 the microphysical processes involved. We plan to conduct some of the research in the
615 future.

616

617 **Acknowledgements :** This work was primarily supported by the National Fundamental
618 Research 973 Program of China (2013CB430101) the National Natural Science
619 Foundation of China (grants 41275031 , 41322032 and 41475015) and Social Common
620 Wealth Research Program (GYHY201006007). Observational data used in this study
621 were collected by a National 973 Project (2013CB430101). Due to its data policy, the
622 DSD and MRR data cannot be released publically until 2018. Special requests for the
623 data can be made at <http://scw973.nju.edu.cn/> or contacting the project office at
624 yang.zhengwei@nju.edu.cn. After 2018, the data of this paper will be uploaded to

625 <http://www.nersc.gov/users/science-gate-ways/> for public sharing. We also thank the
626 Editor and three anonymous reviewers for their valuable suggestions that improved our
627 paper.

628

629 **References**

- 630 Atlas, D., R. Srivastava, and R. S. Sekhon (1973), Doppler radar characteristics of precipitation at
631 vertical incidence, *Reviews of Geophysics*, 11(1), 1-35.
- 632 Aydin, K., and V. Giridhar (1992), C-band dual-polarization radar observables in rain, *Journal of*
633 *Atmospheric and Oceanic Technology*, 9(4), 383-390.
- 634 Blyth, A. M., J. H. Lowenstein, Y. Huang, Z. Cui, S. Davies, and K. S. Carslaw (2013), The production
635 of warm rain in shallow maritime cumulus clouds, *Quarterly Journal of the Royal Meteorological Society*,
636 139(670), 20-31.
- 637 Brandes, E. A., G. Zhang, and J. Vivekanandan (2002), Experiments in rainfall estimation with a
638 polarimetric radar in a subtropical environment, *Journal of Applied Meteorology*, 41(6), 674-685.
- 639 Bringi, V., and V. Chandrasekar (2001), *Polarimetric Doppler weather radar: principles and*
640 *applications*, Cambridge University Press.
- 641 Bringi, V., V. Chandrasekar, J. Hubbert, E. Gorgucci, W. L. Randeu, and M. Schoenhuber (2003),
642 Raindrop Size Distribution in Different Climatic Regimes from Disdrometer and Dual-Polarized Radar
643 Analysis, *Journal of the Atmospheric Sciences*, 60(2), 354-365.
- 644 Bringi, V., M. Thurai, K. Nakagawa, G. HUANG, T. KOBAYASHI, A. ADACHI, H. HANADO, and S.
645 SEKIZAWA (2006), Rainfall Estimation from C-Band Polarimetric Radar in Okinawa, Japan: Comparisons
646 with 2D-Video Disdrometer and 400MHz Wind Profiler, *Journal of the Meteorological Society of Japan*.
647 *Ser. II*, 84(4), 705-724.
- 648 Cao, Q., G. Zhang, E. A. Brandes, and T. J. Schuur (2010), Polarimetric radar rain estimation through
649 retrieval of drop size distribution using a Bayesian approach, *Journal of Applied Meteorology and*
650 *Climatology*, 49(5), 973-990.
- 651 Cao, Q., G. Zhang, E. Brandes, T. Schuur, A. Ryzhkov, and K. Ikeda (2008), Analysis of video
652 disdrometer and polarimetric radar data to characterize rain microphysics in Oklahoma, *Journal of*
653 *Applied Meteorology and Climatology*, 47(8), 2238-2255.
- 654 Carbone, R., J. Tuttle, D. Ahijevych, and S. Trier (2002), Inferences of predictability associated with
655 warm season precipitation episodes, *Journal of the Atmospheric Sciences*, 59(13), 2033-2056.
- 656 Cha, J.-W., K.-H. Chang, S. S. Yum, and Y.-J. Choi (2009), Comparison of the bright band
657 characteristics measured by Micro Rain Radar (MRR) at a mountain and a coastal site in South Korea,
658 *Advances in Atmospheric Sciences*, 26(2), 211-221.
- 659 Chandrasekar, V., R. Meneghini, and I. Zawadzki (2003), Global and local precipitation
660 measurements by radar, *Meteorological Monographs*, 30(52), 215-215.
- 661 Chen, B., J. Yang, and J. Pu (2013), Statistical Characteristics of Raindrop Size Distribution in the
662 Meiyu Season Observed in Eastern China, *Journal of the Meteorological Society of Japan*, 91(2), 215-
663 227.
- 664 Chen, Y., and P. Lin (2009), The Characteristic of Drop Size Distribution During SoWMEX (in Chinese),
665 MS thesis, 68 pp., Inst. of Atmos. Phys., Natl. Cent. Univ., Chungli, Taiwan.
- 666 Ding, Y., and J. C. Chan (2005), The East Asian summer monsoon: an overview, *Meteorology and*
667 *Atmospheric Physics*, 89(1-4), 117-142.
- 668 Fabry, F., and I. Zawadzki (1995), Long-term radar observations of the melting layer of precipitation
669 and their interpretation, *Journal of the atmospheric sciences*, 52(7), 838-851.
- 670 Glickman, T. S. (2000), *Glossary of Meteorology*, edited, Amer. Meteor. Soc.
- 671 Hamada, A., Y. N. Takayabu, C. Liu, and E. J. Zipser (2015), Weak linkage between the heaviest
672 rainfall and tallest storms, *Nature communications*, 6.

673 Hence, D. A., and R. A. Houze Jr (2011), Vertical structure of hurricane eyewalls as seen by the
674 TRMM Precipitation Radar, *Journal of the Atmospheric Sciences*, 68(8), 1637-1652.

675 Hu, Z., and R. Srivastava (1995), Evolution of raindrop size distribution by coalescence, breakup,
676 and evaporation: Theory and observations, *Journal of the atmospheric sciences*, 52(10), 1761-1783.

677 Ishimaru, A. (1991), *Electromagnetic wave propagation, radiation, and scattering*, 637 pp.,
678 Prentice-Hall.

679 Johnson, R. H., T. M. Rickenbach, S. A. Rutledge, P. E. Ciesielski, and W. H. Schubert (1999), Trimodal
680 characteristics of tropical convection, *Journal of climate*, 12(8), 2397-2418.

681 Löffler-Mang, M., and J. Joss (2000), An optical disdrometer for measuring size and velocity of
682 hydrometeors, *Journal of Atmospheric and Oceanic Technology*, 17(2), 130-139.

683 Lee, G. W. (2006), Sources of Errors in Rainfall Measurements by Polarimetric Radar: Variability of
684 Drop Size Distributions, Observational Noise, and Variation of Relationships between R and Polarimetric
685 Parameters, *Journal of Atmospheric and Oceanic Technology*, 23(8), 1005-1028.

686 Liu, J., Y. Zheng, Z. Li, and M. Cribb (2011), Analysis of cloud condensation nuclei properties at a
687 polluted site in southeastern China during the AMF - China Campaign, *Journal of Geophysical Research:*
688 *Atmospheres (1984 - 2012)*, 116(D16).

689 Liu, P., C. Y. Li, Y. Wang, and Y. F. Fu (2012), Climatic characteristics of convective and stratiform
690 precipitation over the Tropical and Subtropical areas as derived from TRMM PR, *Science China Earth*
691 *Sciences*, 56(3), 375-385.

692 Lowenstein, J. H., A. M. Blyth, S. Davies, and K. S. Carslaw (2007), The production of warm rain in
693 shallow cumulus clouds, University of Leeds.

694 Marshall, J. S., and W. M. K. Palmer (1948), The distribution of raindrops with size, *Journal of*
695 *meteorology*, 5(4), 165-166.

696 Masunaga, H., and C. D. Kummerow (2006), Observations of tropical precipitating clouds ranging
697 from shallow to deep convective systems, *Geophysical research letters*, 33(16).

698 May, P., V. Bringi, and M. Thurai (2011), Do we observe aerosol impacts on DSDs in strongly forced
699 tropical thunderstorms?, *Journal of the Atmospheric Sciences*, 68(9), 1902-1910.

700 Milbrandt, J., and M. Yau (2005), A multimoment bulk microphysics parameterization. Part II: A
701 proposed three-moment closure and scheme description, *Journal of the atmospheric sciences*, 62(9),
702 3065-3081.

703 Peters, G., B. Fischer, and T. Andersson (2002), Rain observations with a vertically looking Micro
704 Rain Radar (MRR), *Boreal environment research*, 7(4), 353-362.

705 Rosenfeld, D., and C. W. Ulbrich (2003), Cloud microphysical properties, processes, and rainfall
706 estimation opportunities, *Radar and Atmospheric Science: A Collection of Essays in Honor of David Atlas*,
707 *Meteor. Monogr*, 52, 237-258.

708 Rosenfeld, D., D. B. Wolff, and D. Atlas (1993), General probability-matched relations between
709 radar reflectivity and rain rate, *Journal of applied meteorology*, 32(1), 50-72.

710 Rosenfeld, D., U. Lohmann, G. B. Raga, C. D. O'Dowd, M. Kulmala, S. Fuzzi, A. Reissell, and M. O.
711 Andreae (2008), Flood or drought: how do aerosols affect precipitation?, *science*, 321(5894), 1309-1313.

712 Ryzhkov, A. V., S. E. Giangrande, and T. J. Schuur (2005), Rainfall estimation with a polarimetric
713 prototype of WSR-88D, *Journal of Applied Meteorology*, 44(4), 502-515.

714 Schönhuber, M., G. Lammer, and W. Randeu (2007), One decade of imaging precipitation
715 measurement by 2D-video-distrometer, *Advances in Geosciences*, 10(10), 85-90.

716 Streets, D. G., C. Yu, Y. Wu, M. Chin, Z. Zhao, T. Hayasaka, and G. Shi (2008), Aerosol trends over

717 China, 1980–2000, *Atmospheric Research*, 88(2), 174-182.

718 Sun, J. (2005), Initialization and numerical forecasting of a supercell storm observed during STEPS,
719 *Monthly weather review*, 133(4), 793-813.

720 Tang, Q., H. Xiao, C. Guo, and L. Feng (2014), Characteristics of the raindrop size distributions and
721 their retrieved polarimetric radar parameters in northern and southern China, *Atmospheric Research*,
722 135, 59-75.

723 Tao, S.-Y., and L.-X. Chen (1987), A review of recent research on the East Asian summer monsoon
724 in China, *Monsoon Meteorology*.

725 Tao, W. K., J. P. Chen, Z. Li, C. Wang, and C. Zhang (2012), Impact of aerosols on convective clouds
726 and precipitation, *Reviews of Geophysics*, 50(2).

727 Testud, J., S. Oury, R. A. Black, P. Amayenc, and X. Dou (2001), The Concept of “Normalized”
728 Distribution to Describe Raindrop Spectra: A Tool for Cloud Physics and Cloud Remote Sensing, *Journal*
729 *of Applied Meteorology*, 40(6), 1118-1140.

730 Thompson, E. J., S. A. Rutledge, B. Dolan, and M. Thurai (2015), Drop size distributions and radar
731 observations of convective and stratiform rain over the equatorial Indian and West Pacific Oceans,
732 *Journal of the Atmospheric Sciences*(2015).

733 Tokay, A., and D. A. Short (1996), Evidence from Tropical Raindrop Spectra of the Origin of Rain
734 from Stratiform versus Convective Clouds, *Journal of Applied Meteorology*, 35(3), 355-371.

735 Tokay, A., P. G. Bashor, E. Habib, and T. Kasparis (2008), Raindrop size distribution measurements
736 in tropical cyclones, *Monthly Weather Review*, 136(5), 1669-1685.

737 Tokay, A., W. A. Petersen, P. Gatlin, and M. Wingo (2013), Comparison of raindrop size distribution
738 measurements by collocated disdrometers, *Journal of Atmospheric and Oceanic Technology*, 30(8),
739 1672-1690.

740 Tsai, C.-L., and C.-K. Yu (2012), Intercomparison Analysis for Micro Rain Radar Observations (in
741 Chinese), *atmospheric Science*, 40(2), 109-134.

742 Ulbrich, C. W. (1983), Natural Variations in the Analytical Form of the Raindrop Size Distribution, *J*
743 *Clim Appl Meteorol*, 22(10), 1764-1775.

744 Wen, L., S. Liu, K. Zhao, Y. Li, and L. Li (2015), Precision Evaluation of Micro Rain Radar Observation
745 in Two Precipitation Events (in Chinese), *Meteorological Monthly*, 41(5), 577-587.

746 Xu, W., E. J. Zipser, and C. Liu (2009), Rainfall characteristics and convective properties of mei-yu
747 precipitation systems over South China, Taiwan, and the South China Sea. Part I: TRMM observations,
748 *Monthly Weather Review*, 137(12), 4261-4275.

749 You, C. H., M. Y. Kang, D. I. Lee, and H. Uyeda (2014), Rainfall estimation by S - band polarimetric
750 radar in Korea. Part I: preprocessing and preliminary results, *Meteorological Applications*.

751 Yu, R., and J. Li (2012), Hourly rainfall changes in response to surface air temperature over eastern
752 contiguous China, *Journal of Climate*, 25(19), 6851-6861.

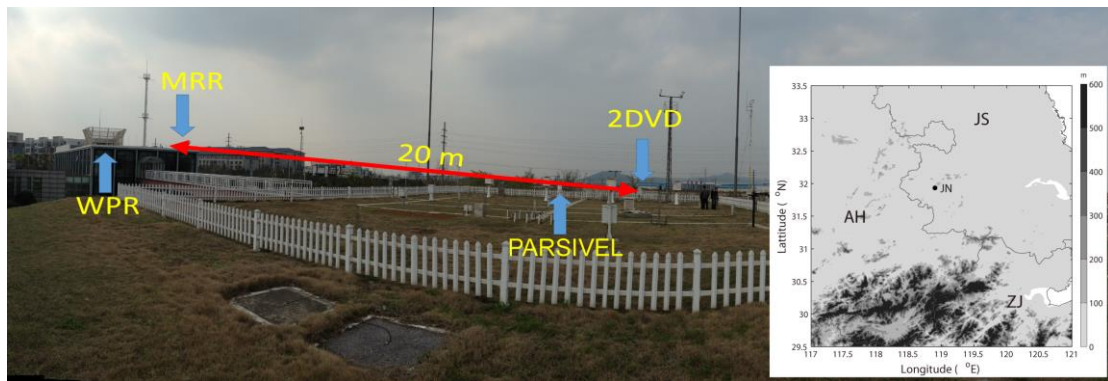
753 Yuter, S. E., and R. A. Houze Jr (1995), Three-dimensional kinematic and microphysical evolution of
754 Florida cumulonimbus. Part II: Frequency distributions of vertical velocity, reflectivity, and differential
755 reflectivity, *Monthly weather review*, 123(7), 1941-1963.

756 Zhang, G., J. Vivekanandan, and E. Brandes (2001), A method for estimating rain rate and drop size
757 distribution from polarimetric radar measurements, *Geoscience and Remote Sensing, IEEE Transactions*
758 *on*, 39(4), 830-841.

759 Zhang, G., J. Sun, and E. A. Brandes (2006), Improving parameterization of rain microphysics with
760 disdrometer and radar observations, *Journal of the atmospheric sciences*, 63(4), 1273-1290.

763 **List of figures**

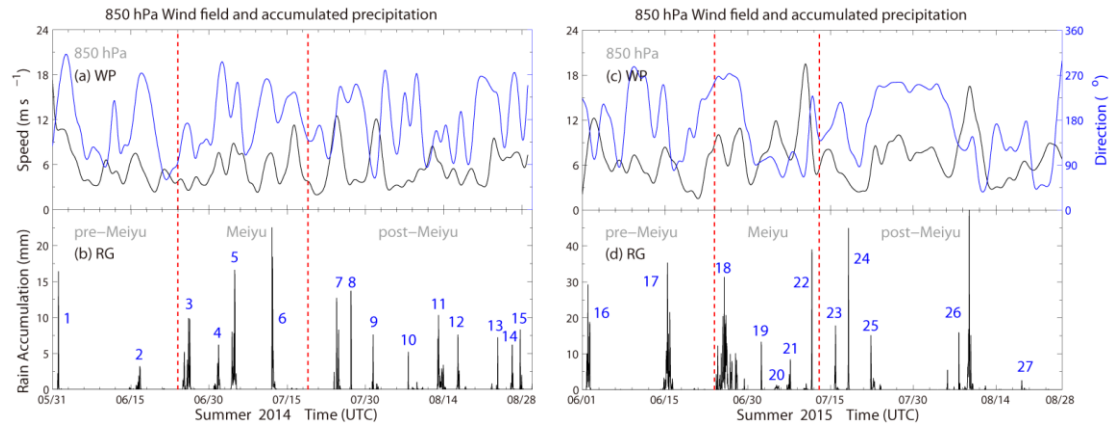
764



765

766 Fig. 1. Field view of the Jiangning site (JN), displaying the relative positions of the
767 Micro-rain radar (MRR), the Wind profiler radar (WPR), the 2D-video disdrometer
768 (2DVD) and the PARSIVEL disdrometer. The inset figure presents the local topography
769 around the JN site.

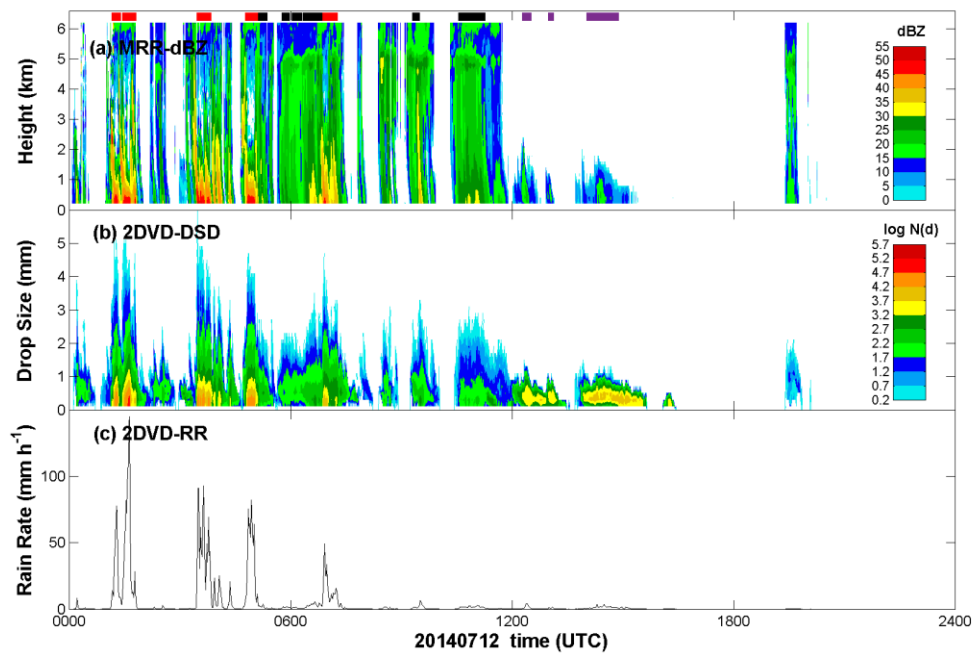
770



771

772 Fig. 2. The observed wind speed and direction by WPR and hourly rainfall by RG from
 773 summer 2014 and 2015. The red vertical dashed lines separate the time period into
 774 segments of pre-Meiyu, Meiyu and post-Meiyu. (a) Wind speed (black line) and wind
 775 direction (blue line); (b) time series of 27 precipitation episodes.

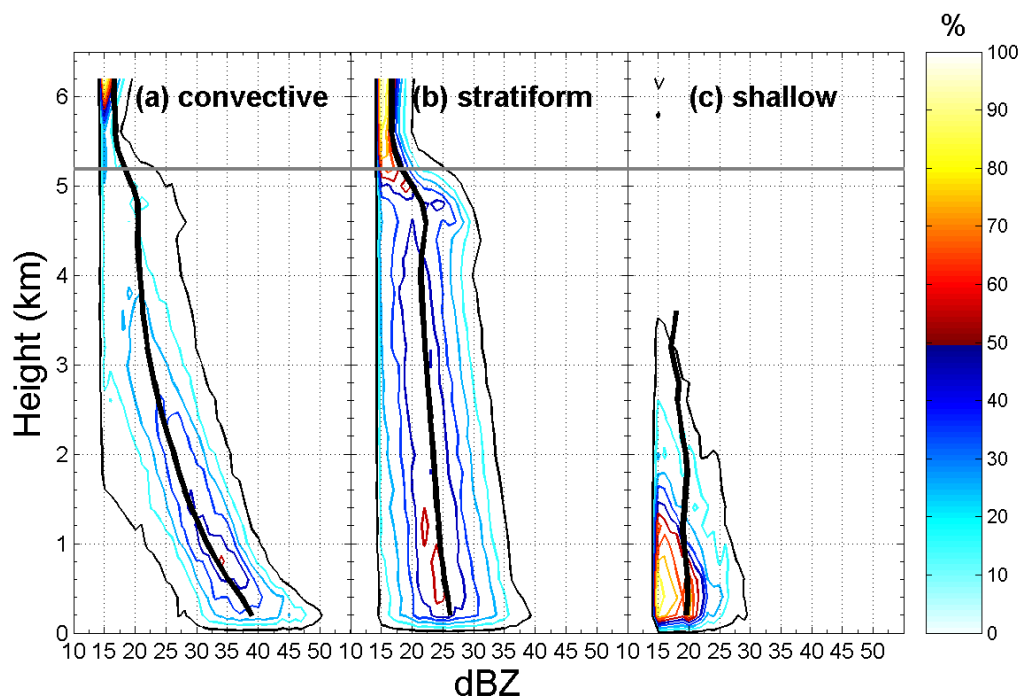
776



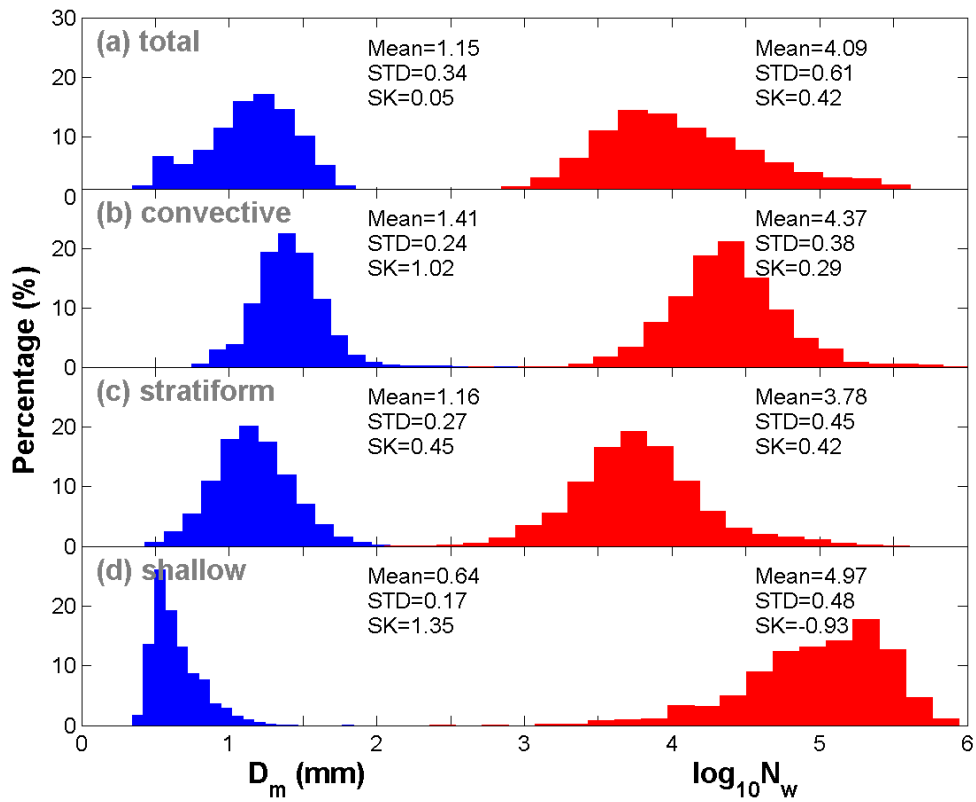
777

778 Fig. 3. The vertical profile of reflectivity from the MRR and the time series of the DSDs
 779 calculated from the 2DVD from 0000 to 2400 UTC 12 Jul 2014. (a) The color shading
 780 represents the vertical profile of reflectivity observed by the MRR. The y-axis
 781 represents the altitude. The classified convective, stratiform and shallow samples are
 782 illustrated by the red, black and purple bars on the top of the diagram. (b) The color
 783 shading represents the DSD in logarithmic units of $\text{mm}^{-1} \text{m}^{-3}$. The y-axis indicates the
 784 equivolume diameter (mm) of raindrops. (c) The black line represents rain rate
 785 calculated from the DSDs.

786



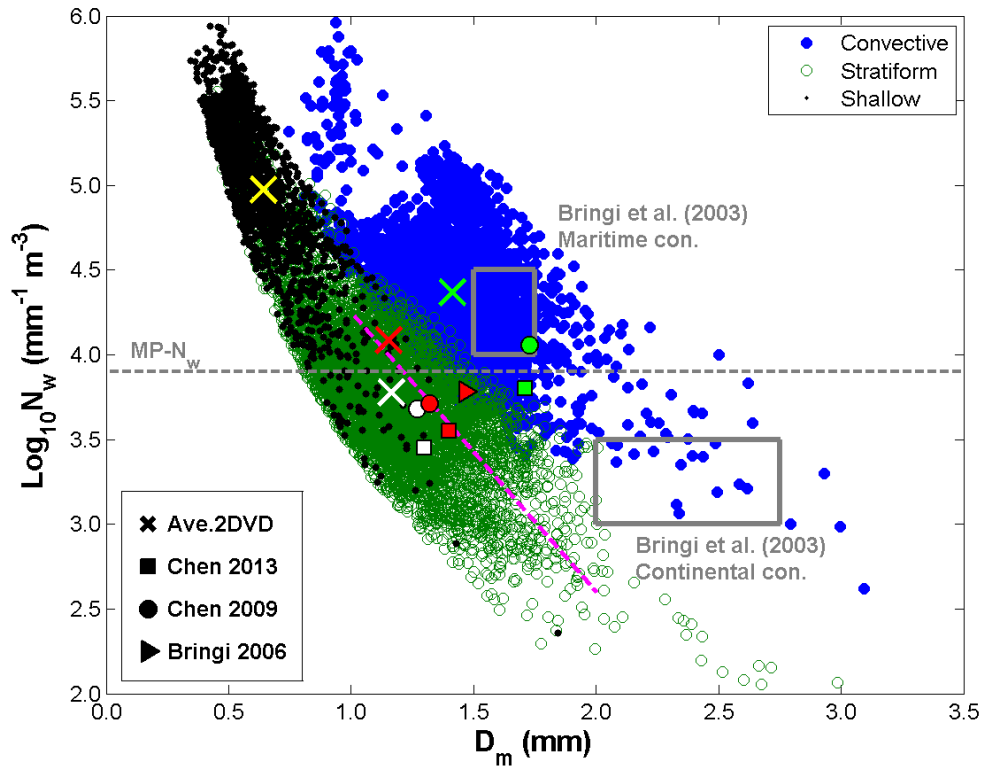
787
 788 Fig. 4. Vertical profiles of reflectivity (>15 dBZ) for different rain types. Contours
 789 represent the frequency of occurrence relative to the maximum absolute frequency in
 790 the data sample represented in the CFAD, contoured every 10% with the minimum of
 791 contour-level at 5%. The ordinate of the CFAD is altitude (200-m bins) and the abscissa
 792 is reflectivity (dBZ, 1-dB bins). The black bold line that goes through each subplot
 793 represents the mean value of reflectivity. The gray line represents the mean level of the
 794 0 °C isotherm obtained from the in situ sounding data.
 795



796

797 Fig. 5. Histogram of D_m and $\log_{10} N_w$ for (a) the total categorized dataset, (b) convective
 798 subset, (c) stratiform subset, and (d) shallow subset. Mean values, standard deviation
 799 (STD), and skewness (SK) are also shown in the respective panels.

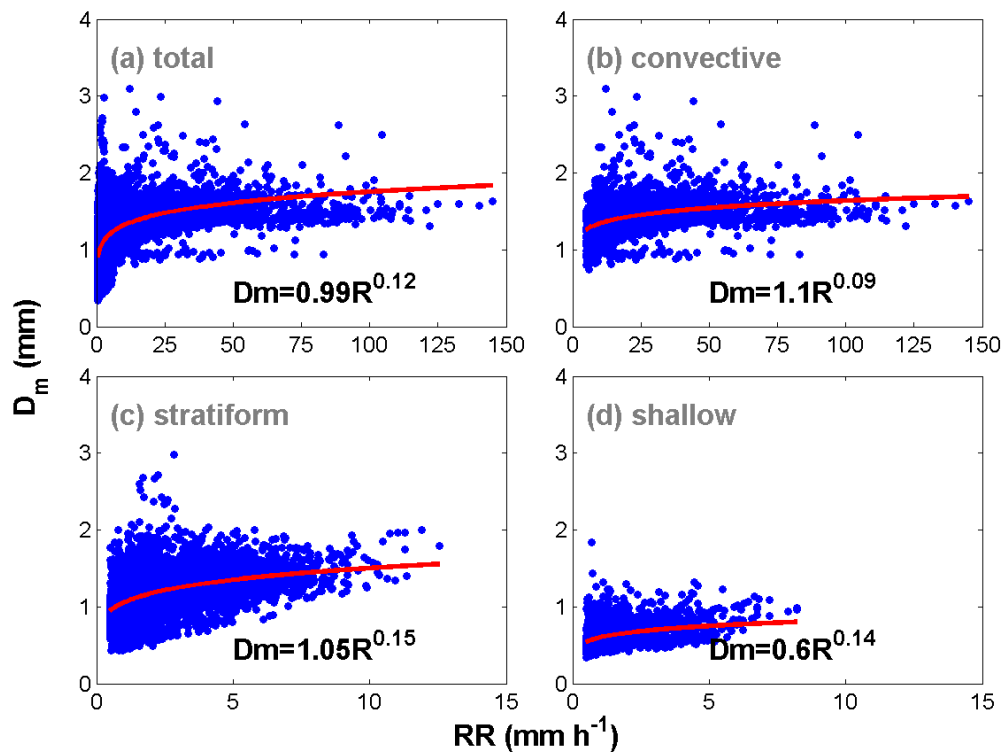
800



801

802 Fig. 6. Scatter plot of $\log_{10} N_w$ versus D_m for convective (blue filled circles), stratiform
 803 (green hollow circles) and shallow (black dots) rain types. The two gray rectangles
 804 correspond to the maritime and continental convective clusters reported by Bringi et al.
 805 [2003]. The square boxes, circles, and triangle represent the averaged values various
 806 types of rain, from Chen et al. [2013], Chen and Lin [2009], and Bringi et al. [2006],
 807 respectively. The red, green, white and yellow colors of these symbols are for the total
 808 categorized dataset, convective, stratiform and shallow rain, respectively. The magenta
 809 dashed line is that of Bringi et al. [2003] for stratiform rain.

810



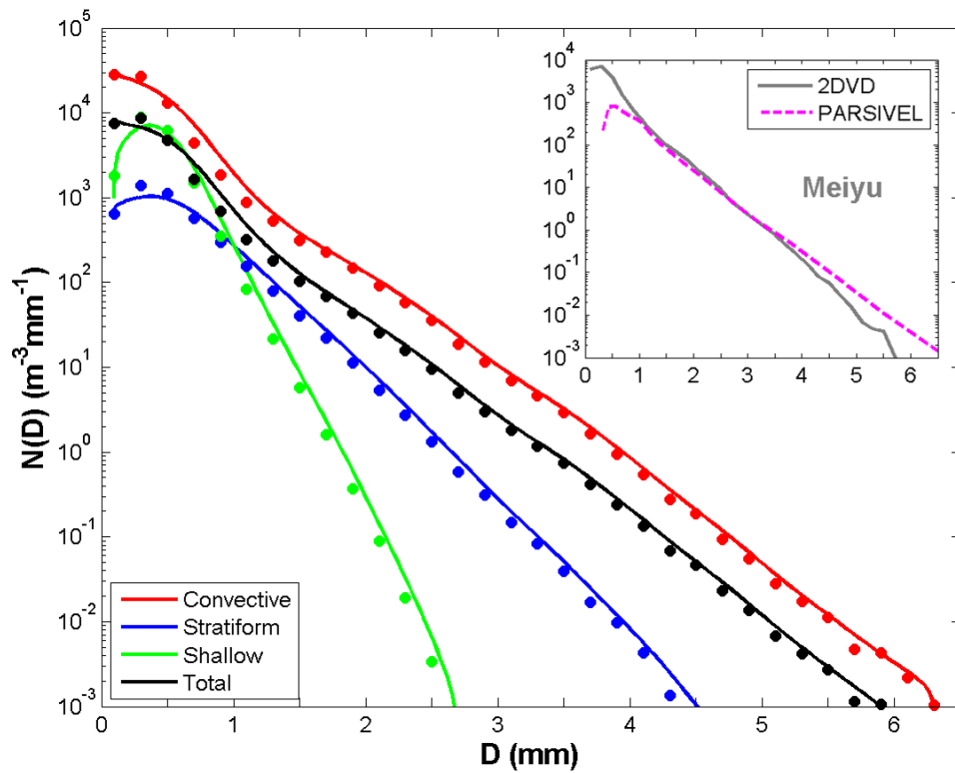
811

812 Fig. 7. Scatter plots of D_m and rain rate (RR) for (a) the total categorized dataset, (b)

813 convective subset, (c) stratiform subset, and (d) shallow subset. The fitted power-law

814 relationships using a least-squares method are provided in each panel.

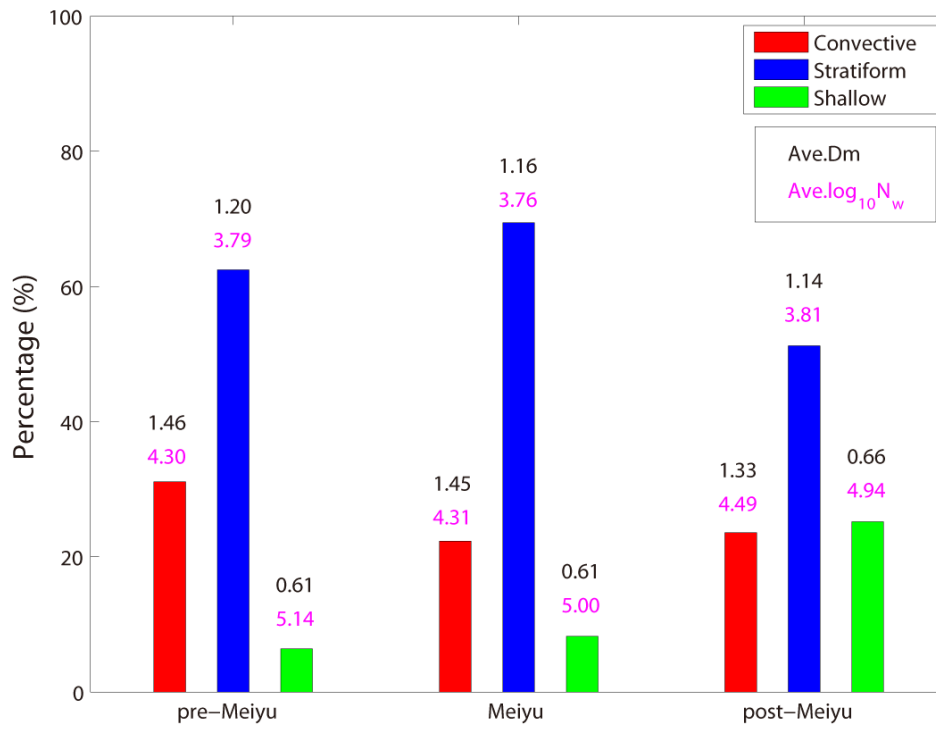
815



816

817 Fig. 8. Composite raindrop spectrum curves (fitted to the observations) for the
 818 convective, the stratiform and the shallow rain types, as well as for the total categorized
 819 dataset. The composite spectra of Meiyu period obtained from our 2DVD and
 820 PARSIVEL disdrometers are also provided at the upper right corner for reference.

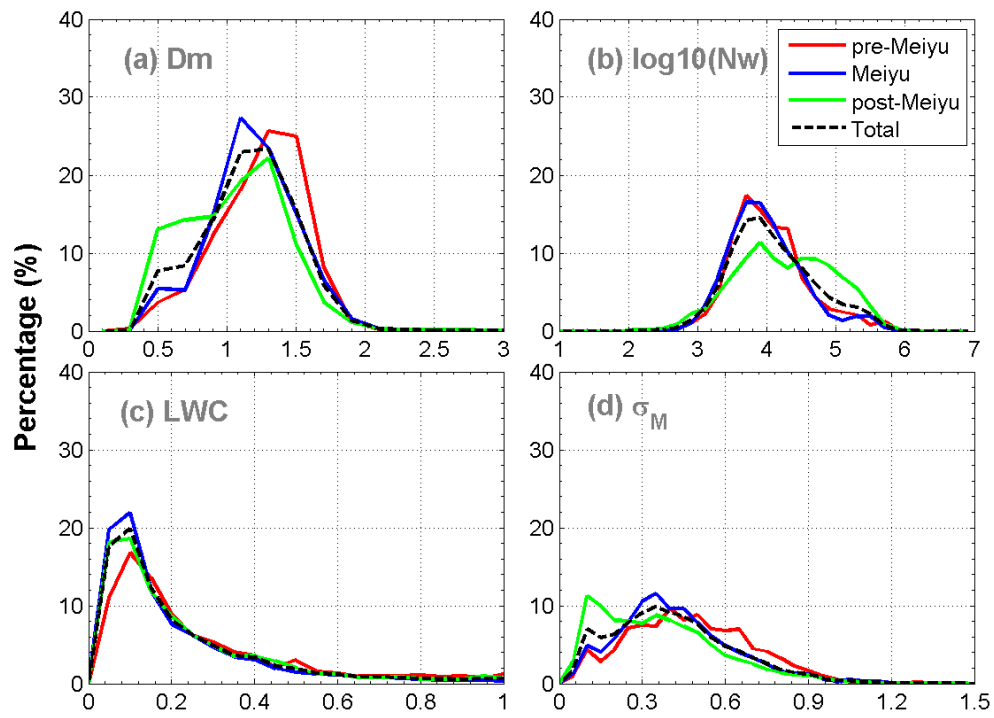
821



822

823 Fig. 9. The percentage occurrence of different rain types during different precipitation
 824 periods. Black and magenta numbers represent average values of D_m and $\text{Log}_{10} N_w$.

825

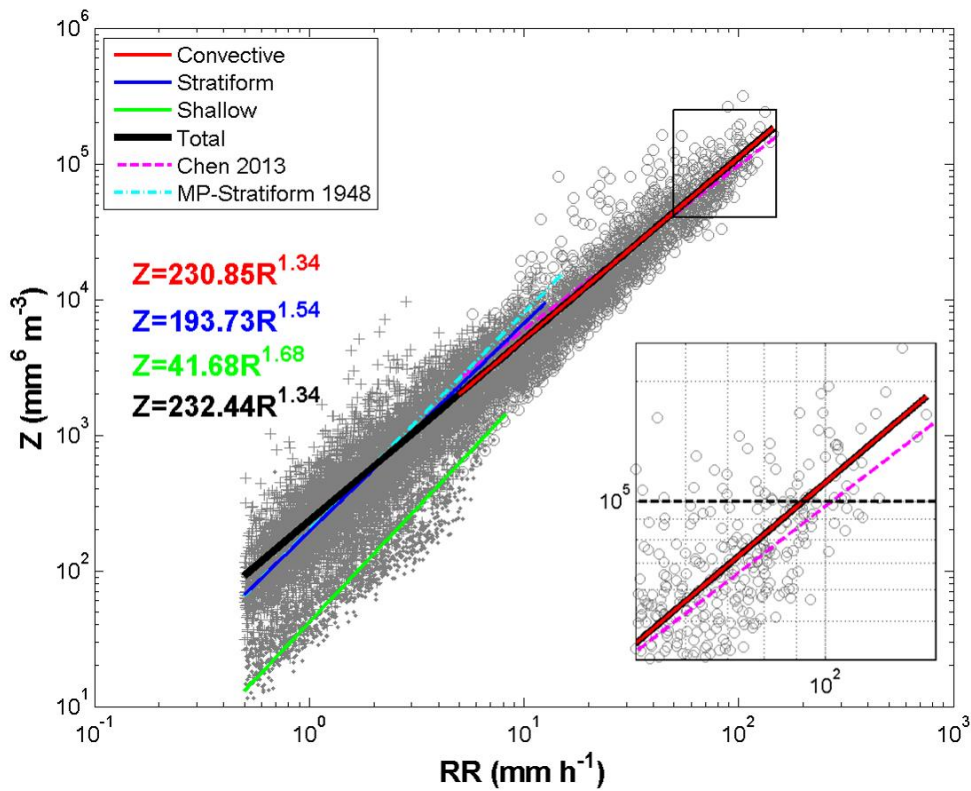


826

827 Fig. 10. The occurrence frequencies of various parameters computed from the DSDs.

828 (a) D_m , (b) $\log_{10} N_w$ (c) LWC and (d) σ_m .

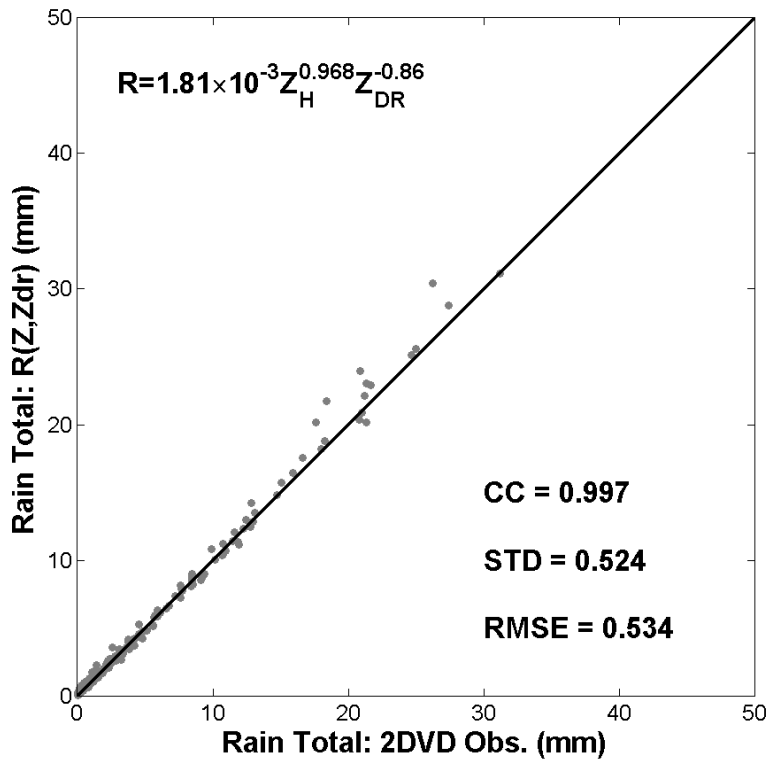
829



830

831 Fig. 11. Scatter plots of Z - R values for convective (gray circles), stratiform (gray plus
 832 signs) and shallow rain (gray dots). The fitted power-law relationships of convective,
 833 stratiform and shallow rain types in the form of $Z=AR^b$ are shown in red, blue and green
 834 solid lines. The coefficient and exponent values of the fitted power-law equations are
 835 provided. The black solid line represents the Z - R relationship for the total categorized
 836 dataset. The relation for continental-stratiform rain [Marshall and Palmer, 1948] and
 837 Meiyu-convective rain [Chen et al., 2013] are provided in dashed cyan and magenta
 838 lines, respectively. The inset plot represents the amplified black rectangle region at the
 839 upper right corner.

840



841
 842 Fig. 12. Scatter plots of 2DVD observed hourly rainfall against rainfall amounts
 843 obtained from the rainfall estimation relationship $R(Z_H, Z_{DR})$. Data came from the
 844 measured DSDs at Jiangning site assuming a Brandes drop shape. Some important
 845 statistical parameters are summarized. CC, STD, RMSE are the correlation coefficient,
 846 standard deviation and root mean square error of rainfall estimate, respectively.
 847

848 **List of table**

849

850 Table 1. Precipitation episodes used for the present study and accumulated precipitation

851

Episode no.	Date	Accumulated precipitation (mm)	Samples (min)	Mean rain rate (mm h ⁻¹)	Max rain rate (mm h ⁻¹)
1	31 May-1 Jun 2014	26.5	189	8.4	88.7
2	16 Jun 2014	17.7	259	4.1	16.6
3	24-27 Jun 2014	67.2	858	4.7	43.4
4	1-2 Jul 2014	30.0	399	4.5	37.4
5	4-5 Jul 2014	83.2	1005	5.0	114.4
6	12 Jul 2014	72.0	321	13.5	145.1
7	24-25 Jul 2014	40.2	337	7.2	26.2
8	27 Jul 2014	25.5	113	13.5	72.8
9	31 Jul-1 Aug 2014	15.1	101	9.0	70.5
10	8-9 Aug 2014	8.2	89	5.5	10.6
11	12-14 Aug 2014	56.5	642	5.3	47.6
12	16-18 Aug 2014	22.3	238	5.6	36.9
13	24 Aug 2014	8.7	20	26.1	52.4
14	26-27 Aug 2014	16.4	220	4.5	18.2
15	28-30 Aug 2014	16.7	138	7.3	104.2
16	1-2 Jun 2015	143.8	600	14.4	122.1
17	15-17 Jun 2015	171.0	894	11.5	114.7
18	25-30 Jun 2015	372.6	1706	13.1	110.8
19	3 Jul 2015	22.7	41	33.2	81.8
20	5-6 Jul 2015	10.1	472	1.3	3.8
21	7-8 Jul 2015	22.0	335	3.9	63.9
22	11 Jul 2015	6.8	147	2.7	17.9
23	16-19 Jul 2015	122.8	473	15.6	106.1
24	23 Jul 2015	39.1	423	5.5	88.1
25	24-25 Jul 2015	3.4	35	5.8	16.4
26	8-10 Aug 2015	196.4	919	12.8	114.2
27	19-20 Aug 2015	5.2	27	12.2	35.1

852

853

854 Table 2. Frequency of precipitation of the classified rain types. The percentage refers to the
855 contribution of each rain type to the total categorized rainfall amount.
856

Rain type	Samples (min)	<i>R</i> (mm h ⁻¹)	Accumulated Rainfall (mm)	Percentage (%)
Convective	2701	24.44	1100.2	77.5
Stratiform	6882	2.35	269.4	19.0
Shallow	1530	1.95	49.7	3.5
Total	11113	7.66	1419.3	100

857
858

859 Table 3. Integral rain parameters derived from the composite raindrop spectra. Parameters N_T , N_w ,
 860 LWC , R , D_m and D_0 are the total raindrop concentration, generalized raindrop concentration, liquid
 861 water content, rain rate, mass-weighted mean diameter, and maximum raindrop diameter,
 862 respectively.

863

Rain type	Samples (min)	N_T (m^{-3})	$\log_{10} N_w$ ($m^{-3} mm^{-1}$)	LWC ($g m^{-3}$)	R ($mm h^{-1}$)	D_m (mm)	D_{max} (mm)
Convective	2701	8079	4.37	1.50	24.4	1.41	6.3
Stratiform	6882	627	3.78	0.15	2.3	1.16	4.5
Shallow	1530	2763	4.97	0.21	1.9	0.64	2.9
Total	11113	1432	4.09	0.49	7.7	1.15	6.3

864

865

866 Table. 4. Integral rain parameters derived from the composite raindrop spectra for pre-Meiyu,
 867 Meiyu and post-Meiyu periods. Parameters N_T , N_w , LWC , R , D_m and D_0 are the total raindrop
 868 concentration, generalized raindrop concentration, liquid water content, rain rate, mass-weighted
 869 mean diameter, and maximum raindrop diameter, respectively.

870

Period	Samples (min)	N_T (m^{-3})	$\log_{10} N_w$ ($m^{-3} mm^{-1}$)	LWC ($g m^{-3}$)	R ($mm h^{-1}$)	D_m (mm)	D_{max} (mm)
pre-Meiyu	1953	1700	4.03	0.57	9.2	1.24	6.3
Meiyu	5323	1184	3.99	0.44	7.2	1.18	5.7
post-Meiyu	3838	1708	4.25	0.50	7.5	1.07	5.9
Total	11113	1432	4.09	0.49	7.7	1.15	6.3

871

872